

# Texture or Linker? Competitive Patterning of Receptor Assembly toward Ultra-Sensitive Impedimetric Detection of Viral Species at Gold-Nanotextured Titanium Surfaces

Wiktorja Lipińska, Adrian Olejnik, Monika Janik, Mateusz Brodowski, Karolina Sapięga, Mattia Pierpaoli, Katarzyna Siuzdak, Robert Bogdanowicz, and Jacek Ryl\*



Cite This: *J. Phys. Chem. C* 2023, 127, 9584–9593



Read Online

ACCESS |



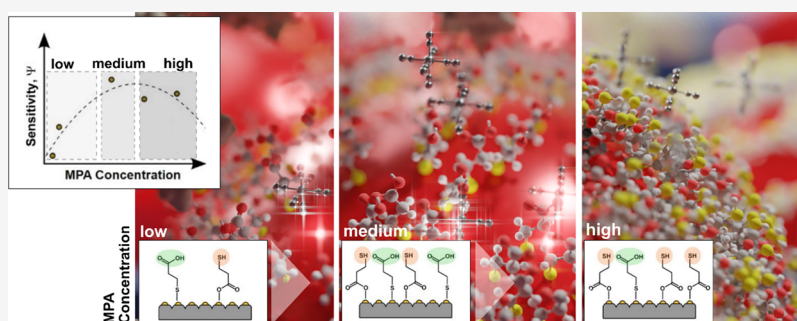
Metrics & More



Article Recommendations



Supporting Information



**ABSTRACT:** In this work, we study the electrodes with a periodic matrix of gold particles patterned by titanium dimples and modified by 3-mercaptopropionic acid (MPA) followed by CD147 receptor grafting for specific impedimetric detection of SARS-CoV-2 viral spike proteins. The synergistic DFT and MM/MD modeling revealed that MPA adsorption geometries on the Au–Ti surface have preferential and stronger binding patterns through the carboxyl bond inducing an enhanced surface coverage with CD147. Control of bonding at the surface is essential for oriented receptor assembling and boosted sensitivity. The complex Au–Ti electrode texture along with optimized MPA concentration is a crucial parameter, enabling to reach the detection limit of ca. 3 ng mL<sup>-1</sup>. Scanning electrochemical microscopy imaging and quantum molecular modeling were performed to understand the electrochemical performance and specific assembly of MPA displaying a free stereo orientation and not disturbed by direct interactions with closely adjacent receptors. This significantly limits nonspecific interceptor reactions, strongly decreasing the detection of receptor-binding domain proteins by saturation of binding groups. This method has been demonstrated for detecting the SARS virus but can generally be applied to a variety of protein–antigen systems. Moreover, the raster of the pattern can be tuned using various anodizing processes at the titania surfaces.

## 1. INTRODUCTION

Electrochemical biosensors are one of the common sensing devices that convert biological processes into electrical signals.<sup>1–3</sup> An electrode is a crucial component in this type of device for the immobilization of biomolecules and the flow of electrons. It plays the role of the transducer as well as the substrate for the receptor. Electrochemical immunosensors are widely utilized due to their multiple benefits over traditional immunoassay techniques, including outstanding sensitivity, rapid detection times, straightforward pretreatment, tiny analyte volumes required, easy apparatus, and no need for manipulation. In addition to being reliable, electrochemical biosensors are simple to miniaturize and offer wide detection limits even when analyte concentrations are low.<sup>4</sup> Offering the detection of several key biomolecules, including glucose, cholesterol, uric acid, lactate, DNA, hemoglobin, blood

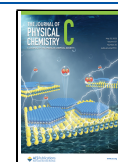
ketones, and others,<sup>5,6</sup> these sensors have enormous potential to heal illnesses brought on by biomolecular imbalances.

A commonly used procedure for increasing the surface loading of the biomolecules is nanostructuring the electrode surface, as this produces a much higher surface-to-volume ratio than flat planes.<sup>7</sup> Tajima et al.<sup>8</sup> controlled the antibody orientation by conjugating a staphylococcal protein to the amino group, including a platform employing tyrosinase. Various plasma polymers deposited at the electrodes could also be applied for patterned biomolecule immobilization forming

Received: January 31, 2023

Revised: April 27, 2023

Published: May 10, 2023



microarray or protein assay devices.<sup>9</sup> Kim et al.<sup>10</sup> manifested that the binding possibility between IgG and antigen was enhanced by controlling the orientation of the IgG through an applied E-field. Nanoparticles are also offering synergistic effects by enhancing the reactant loading capacity and mass transfer to achieve high analytical sensitivity performance.<sup>11,12</sup> Sun et al.<sup>13</sup> studied novel nanotextured (Au, Pd, Pt) microelectrodes for tracking DNA hybridization. There are reports of AuNP heterojunctions with carbon or metal oxides offering, among others, high surface area and specific electronic and electrical conductivity. Several studies conclude an enhancement in biosensor properties by reducing the fouling and improving the electron transfer kinetics.<sup>14,15</sup> Wei et al.<sup>16</sup> indicated an improvement in the performance of a titanium dioxide-modified hemoglobin-based peroxide sensor doped with AuNP. The structured titanium foil with embedded Au nanoparticles and modified with chitosan with entrapped glucose oxidase were utilized for glucose detection.<sup>17,18</sup>

The demand for increasingly low detection limits is often met by proposing highly complex electrode architectures. While successful under laboratory conditions, the manufacturing of these systems is extremely difficult to scale up and commercially manufacture, often having high material and manufacturing costs.<sup>19</sup> The Au–Ti nanotextured electrodes (AuTi-NTE) proposed and previously utilized by our group<sup>17,18</sup> do not possess most of these disadvantages. The substrate fabrication takes advantage of the scalable anodization process that does not require complicated and highly expensive equipment. The electrolyte is based on commonly available compounds, while the whole anodization process can be easily controlled by a computer. All steps are well managed on a technological scale.

The successful detection of macromolecular compounds by electrochemical biosensors largely depends on the specific adsorption of the analyte with a target receptor functionalized on the electrode surface.<sup>7</sup> Surface functionalization enables crucial interfacial characteristics to be tuned. Electrochemical reduction of diazonium salts<sup>20</sup> and oxidation of amine<sup>21</sup> or carboxylate<sup>22</sup> could be utilized to achieve covalent attachment of organic molecules, while other methods include bonding thiols to the surface of various metals.<sup>23</sup> Among the thiols, 3-mercaptopropionic acid (MPA) is one of the most often utilized organic molecules, forming covalent S–Au bonds at the surface of gold. The stability of such a bond is high, thus, it could be used for designing electrochemical sensors. This approach is used in numerous studies on electrochemical biosensors, often proving to be the best possible with high stability and sensitivity.<sup>24,25</sup> The manipulation of complex biomolecular compounds with nanometer precision has critical ramifications for the creation of biomaterial surfaces with exact responses for targeted biosensing. In particular, the development of effective biosensors based on the controlled deposition of biomolecules at the molecular level requires both the understanding and control of the protein/protein and protein/electrode adsorption processes. Furthermore, to limit the nonspecific adsorption at the biosensor surface, various antifouling strategies could be implemented, including bovine serum albumin (BSA) adsorption, increasing the biochemical complexity of the electrode interface.<sup>19</sup>

In this work, we proposed a specific mechanism of receptor assembly toward ultra-sensitive impedimetric detection of viral species at gold-nanotextured titanium electrodes (AuTi-NTE). Insight into the competitive interaction of MPA concentration

and texture of AuTi-NTE allowed for the design of an ultra-sensitive impedimetric detection platform due to the patterning of receptor anchoring. The AuTi-NTE was functionalized utilizing an optimized anodization process followed by AuNP formation toward rastered grafting of the CD147 receptor. Constituting the first step of the functionalization process, MPA anchoring to gold surfaces, driven among others by its concentration or electrode texture, is the key feature that determines the resultant biosensor output. Such an approach has not been reported up to date allowing for tailoring of receptor densities in immunoassay. The synergistic DFT and MM/MD modeling was carried out to reveal the modification mechanism tuned by MPA preferring the carboxyl group for the formation of covalent Au–S bonding. The carboxyl bond MPA molecules induce compact coverage by the CD147 receptor. A developed functionalization strategy enabled to achieve a rapid and highly effective platform for SARS-CoV-2 viral RBD detection.

## 2. MATERIALS AND METHODS

**2.1. Reagents and Biomaterials.** MPA (99%), 1-ethyl-3-(3-dimethylaminopropyl)carbodiimide (EDC), *N*-hydroxysuccinimide (NHS), and BSA were purchased from Sigma Aldrich and used for the modification of the nanostructured gold electrodes. Potassium ferric hexacyanoferrate (iii), potassium hexacyanoferrate (ii) trihydrate, and ethanol were purchased from Chempur. Dipotassium phosphate and monopotassium phosphate for phosphate buffer solution (PBS) were purchased from Stanlab. Double-distilled water (dd H<sub>2</sub>O) was used to prepare all aqueous solutions. Air products delivered refrigerated argon. The biological materials, i.e., the receptor-transmembrane glycoprotein CD147 (972-EMN) (CD147), and the targeted SARS-CoV-2 Spike receptor-binding domain proteins (CHO: 1-534-CV) (RBD), were obtained from R&D Systems. Both proteins were labeled with the C-terminal 6-His tag. All reagents were used without prior purification and stored according to the manufacturer's instructions.

**2.2. Functionalization of the Electrodes.** The studied gold-nanotextured titanium electrodes are composed of rastered Ti dimples packed with a separated gold nanoparticle modified with the CD147 receptor. The complex nanostructure was fabricated applying a three-step process covering (a) anodization to create TiO<sub>2</sub> nanotubes followed by their etching, (b) formation of gold nanoparticles in etched Ti dimples, and (c) modification by the CD147 receptor through an MPA linker.

Thin gold electrodes (Arrandee) and Ti foils (Sigma Aldrich) were used as reference surfaces. After rinsing in ethanol the electrodes were placed in test tubes filled with 700  $\mu$ L of MPA solution in ethanol and were left for 1 h in darkness. Next, the electrodes were placed in 700  $\mu$ L of EDC (50 mM, PBS pH 5.81) and NHS (30 mM, PBS pH 8.01) for 30 min each, with prior rinsing with demineralized water. All previous steps were performed at 25 °C. In the next step, the electrodes were placed horizontally in the fridge (5 °C) and 75  $\mu$ L of CD147 solution (3.4  $\mu$ g mL<sup>-1</sup>, PBS pH 7.4) was placed on the side of the electrode, which was then left for 16 h. In the next step, 75  $\mu$ L of 0.01% (w:w) BSA solution in PBS (pH 7.39) was dripped onto the side of the electrode and left for 5 min.

**2.3. Analytical Methods.** The SARS-CoV-2 RBD solution (75  $\mu$ L), serving as the analyte, was dripped onto the side of the electrode in different concentrations and left for 30 min.

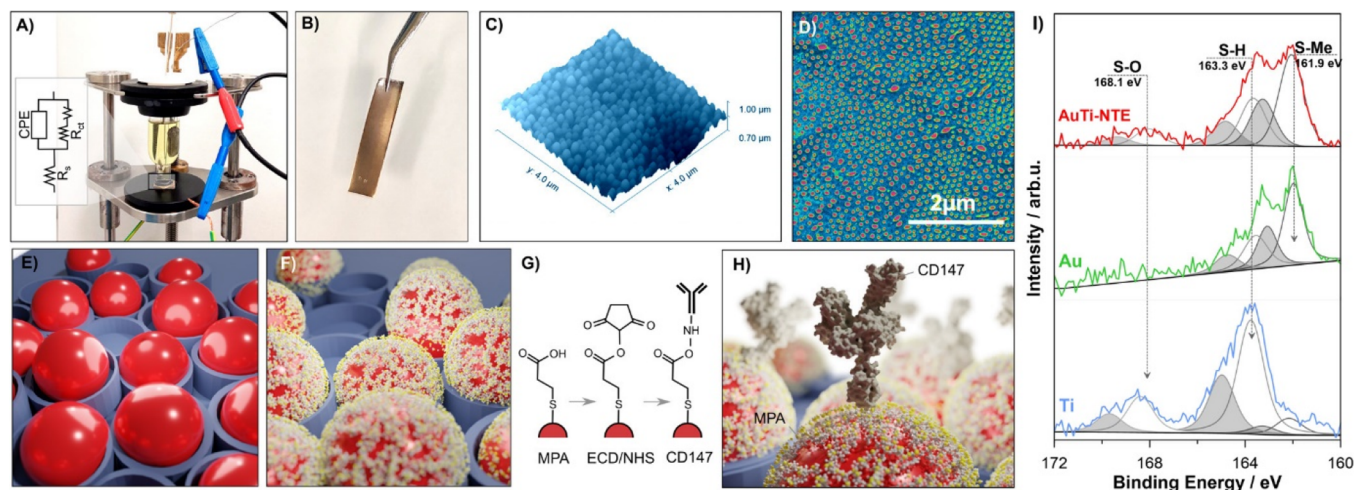


**Figure 1.** (A) electrochemical cell and (B) AuTi-NTE electrode photographs. Topography of as-prepared AuTi-NTE, visualized by: (C) AFM (D) FE-SEM. (E–H) functionalization scheme: (E) unmodified AuTi-NTE, (F) MPA adsorption, (G) consecutive functionalization steps, (H) ready-to-use sensor with CD147 anchored. (I) XPS S2p analysis after modification with MPA.

All studies were performed on an Autolab PGSTAT302N potentiostat/galvanostat (Metrohm). Pt wire served as the counter electrode and Ag|AgCl (3 M KCl) was the reference electrode. All measurements were performed in 5 mL of electrolyte deaerated with argon and containing 2.5 mM  $K_3[Fe(CN)_6]$ , 2.5 mM  $K_4[Fe(CN)_6]$ , and 0.1 M PBS (pH 7.4), unless stated otherwise. The electrolyte-exposed electrode area was 0.5 cm<sup>2</sup>. A photograph of the used electrochemical cell is shown in Figure 1A.

The electrochemical impedance spectroscopy (EIS) studies were conducted at the redox potential obtained from CV (approx. 0.22 V vs Ag|AgCl (3 M KCl)), in the frequency range 10 kHz to 0.1 Hz, 10 points per decade and peak-to-peak amplitude of 10 mV. The impedimetric results were fitted using dedicated software built in the LabView environment and based on the Nelder–Mead algorithm<sup>26</sup> and previously used in similar studies.<sup>27,28</sup> Selection of the electric equivalent circuit (see Figure 1A, inset) is discussed in the SI file, Section 3. Cyclic voltammetry (CV) was performed in the range from –0.30 to 0.65 V with a scan rate of 100 mV s<sup>–1</sup> in triplicate.

Scanning electrochemical microscopy (SECM) measurements were carried out utilizing a commercially available system (Sensolytics GmbH), details previously reported.<sup>28</sup> The tests were conducted using 5 mM  $K_4[Fe(CN)_6]$  dissolved in PBS (pH 7.4). All experiments were performed in feedback mode.

Scanning electron microscope (FE-SEM) imaging of the AuTi-NTE topography was carried out using an FEI Quanta 250 FEG (Thermo Fisher Scientific). The topography of the surfaces was inspected by an atomic force microscope (AFM) (Nanosurf EasyScan 2) in the contact mode regime. The high-resolution X-ray photoelectron spectroscopy (XPS) analyses were carried out with Escalab 250Xi (Thermo Fisher Scientific) using the procedure described earlier.<sup>27</sup>

Density-functional theory (DFT) calculations and Molecular Mechanics/Molecular Dynamics MM/MD computational details are presented in the SI file, Section 1.

### 3. RESULTS AND DISCUSSION

**3.1. Topography and Functionalization Efficacy.** The topography of the studied gold-nanotextured electrode (Figure 1B), imaged by AFM and SEM microscopies, is presented in

Figure 1C,D, respectively. A uniform distribution of AuNPs over the whole Ti substrate was ensured. In our previous studies confirmed by the AFM analysis, AuNPs diameter was estimated to be  $72.6 \pm 4.6$  nm.<sup>18</sup> It should be highlighted that such optimization of dimensions generates the configuration of one nanoparticle per nanodimple. The functionalization protocol, as described in the experimental section, is summarized in Figure 1E–H.

High-resolution XPS studies confirmed MPA modification (as in Figure 1F) and functionalization leading to CD147 anchoring (Figure 1H). Sulfur atoms covalently bonded to a metal surface (AuNP and Au), S2p<sub>3/2</sub> peaking at 161.9 eV,<sup>29,30</sup> are dominant, a feature nearly negligible in the case of Ti surface, where the primary component at 163.3 eV was assigned to physisorbed thiols or thiolates<sup>29,31</sup> (see Figure 1I). Notably, the covalent-to-physisorbed S species ratio in AuTi-NTE is approx. 1.97:1 immediately after exposure to the MPA solution. The XPS spectra for Au4f, Ti2p, N1s, and C1s were presented and discussed in SI, Figure S1. Analysis of the S2p spectra convinced us of two important observations. First, an additional component shifted by +4.8 eV vs physisorbed thiol species was recognized, in particular when MPA adsorbs at the Ti surface. Such a strong shift may only be explained by the presence of electronegative oxygen bonded to sulfur, such as in sulfites or sulfates.<sup>32</sup> The available –SH moieties may be subject to oxidation and aging in the air or aqueous solution,<sup>33,34</sup> where the self-initiated reactions may be further catalyzed by transition metals.<sup>35</sup> Indeed, the proportion of –SO species in the total [S] content is much higher for Ti-based electrodes (Ti sheet 28% and AuTi-NTE 12%) compared to solid Au (below threshold). Second, when analyzing S2p spectra at the Ti sheet, one can notice the negligible share of sulfur atoms covalently bonded to the metal surface. While the presence of –SH moieties was confirmed, the MPA molecules are plausibly physisorbed at the Ti sheet, but may also be covalently bonded to the metal surface through carboxyl groups. The latter is more plausible considering the significant increase in the –CO moieties recognized in the C1s spectra (34.4 for Ti, and 11.1 at % for AuTi-NTE after complete functionalization).

In conclusion, the MPA adsorption at the electrode surface is possible through both thiol and carboxyl species, while the

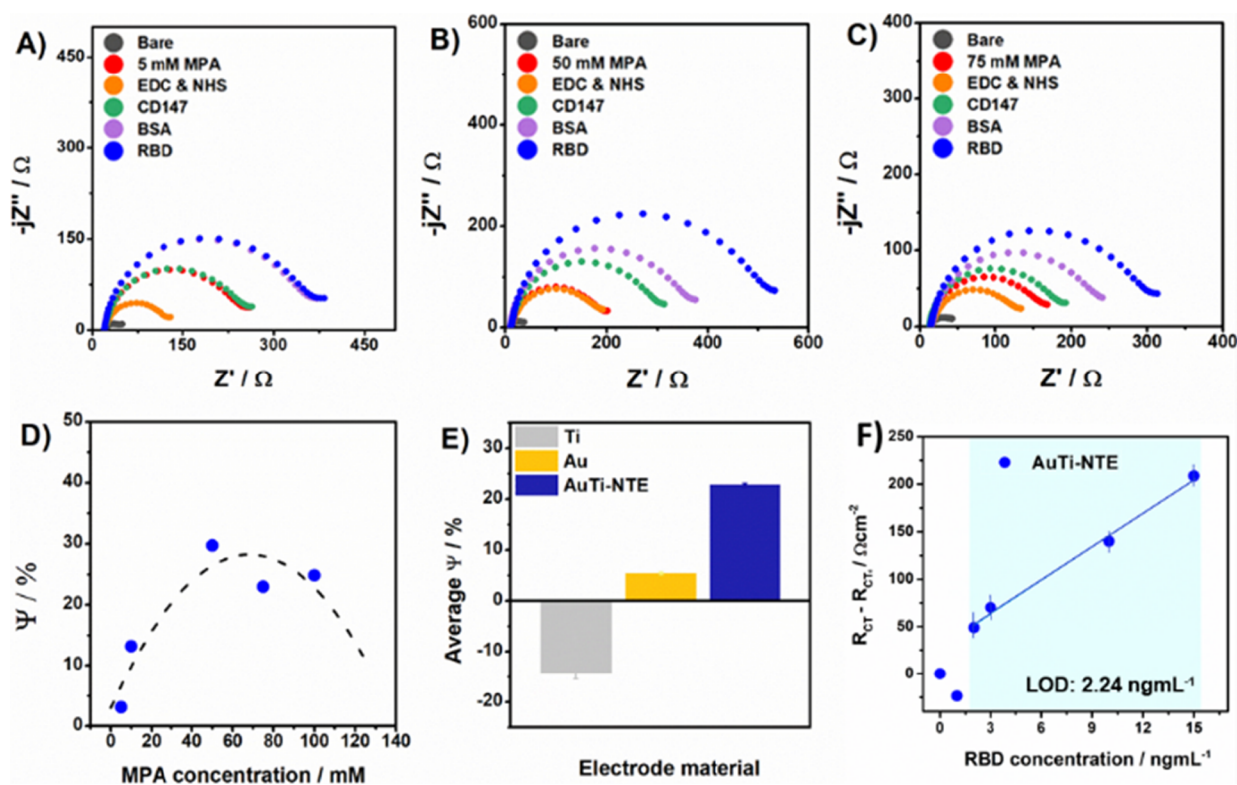


**Figure 2.** (A–C) EIS spectra registered for AuTi-NTEs at each stage of electrode functionalization, at different MPA concentrations: (A) 5; (B) 50; (C) 75 mM; (D) function of sensor response  $\Psi$  changes with the MPA concentration for a SARS-CoV-2 RBD concentration of 15 ng mL<sup>-1</sup>; (E) sensor response comparison between AuTi-NTE, Ti, and Au electrodes (50 mM MPA); (F) SARS-CoV-2 RBD detection range at AuTi-NTE (50 mM MPA). Electrolyte: 0.1 M PBS + 2.5 mM K<sub>3</sub>[Fe(CN)<sub>6</sub>] + 2.5 mM K<sub>4</sub>[Fe(CN)<sub>6</sub>].

latter seems more likely in the case of Ti surfaces based on the XPS analyses. It should be noted that the thiol-electrode connection leads to the successful attachment of the CD147 protein; however, this cannot be accomplished if the MPA molecule is a carboxyl-connected to the electrode surface because the EDC/NHS reactions would not occur.

**3.2. SARS-CoV-2 Detection at AuTi-NTEs and the Effect of the MPA Concentration.** The impedimetric analysis can reveal changes in electrical double-layer capacitance and charge transfer resistance ( $R_{CT}$ ) and provide information on surface heterogeneity. The EIS results obtained for different MPA concentrations, after consecutive functionalization steps and binding the SARS-CoV-2 RBD (5  $\mu$ g mL<sup>-1</sup>) are shown in Figure 2A–C and Supplementary Figure S2.

Upon analyte biomolecule adsorption to the functionalized electrode surface, the electrochemically active surface decreases, hindering the redox process, which is easily observed by an  $R_{CT}$  increase.<sup>36,37</sup>  $R_{CT}$  was then used to estimate sensor performance  $\Psi$ , see SI, Section 3 for details. Most notably, the sensor performance  $\Psi$  strongly depends on the MPA concentration, indicating the key importance of this first functionalization step on the biosensor efficacy. The  $\Psi(c_{MPA})$  function, as shown in Figure 2D, takes a parabola shape, where the highest sensor response is observed at about  $c_{MPA} = 50$  mM and slightly decreases after exceeded. It is expected that, at low concentrations,  $R_{CT}$  of the biosensor will increase proportionally to  $c_{MPA}$  and this trend will last until full electrode surface coverage  $\theta$  by the self-assembled MPA monolayer. This is because the amount of surface carboxyl groups available for EDC/NHS chemistry has a direct impact on the anchored CD147 molecules and the sensor sensitivity to the analyte.

Worsening the biosensor response upon exceeding the MPA concentration sufficient for full surface coverage by its monolayer is, however, unexpected and is a subject of further research. Initially, we were convinced that its origin was in steric hindrance effects or possible electrode blocking due to nonspecific MPA adsorption upon reaching  $\theta = 100\%$ . It is worth noting that the decrease of the biosensor response  $\Psi$  is not easy to track just by measuring  $R_{CT}$  during the corresponding functionalization step, where  $R_{CT}$  was decreasing with the  $c_{MPA}$  increase (see Supplementary Figure S3).

The biosensor response  $\Psi$  of the AuTi-NTE (30% at 50 mM MPA) was nearly 5 $\times$  higher compared to the solid Au electrode (see Figure 2E). The XPS analyses pointed to the conclusion that due to the formation of covalent bonds by carboxyl groups, the MPA molecules at the Ti surface most likely do not play an active role in CD147 anchoring. A similar conclusion may be drawn based on the decrease in biosensor  $R_{CT}$  and negative response  $\Psi$  observed after the functionalization of the Ti sheet. On the other hand, the total share of gold at the surface of the AuTi-NTE is only 17.59% based on the analysis of the SEM micrograph from Figure 1D with the dominant contribution of Au NP size in dimpled Ti surface between 70 and 85 nm (details in SI, Figure S5); thus, the outstanding increase of  $\Psi$  compared to solid Au cannot be explained by the increase in electrochemically active surface area. The impact of the electrocatalytic effect and the AuTi-NTE geometric factor is to be considered. The EIS results obtained after the functionalization of solid Au and Ti electrodes are presented in SI, Figure S4 and Table S1. The relationship between  $R_{CT}$  increase upon RBD anchoring vs the RBD concentration is given in Figure 2F. The limit of

detection (LOD) was determined using the relation:  $(3.3 \times \text{SD})/b$ , where SD is the standard deviation and  $b$  is attributed to the slope of the calibration curve.<sup>38</sup> The LOD for the AuTi-NTE electrode reaches ca.  $3 \text{ ng mL}^{-1}$ .

**3.3. DFT Simulation Study of MPA Adsorption.** DFT computations were utilized to explain the observed phenomena experimentally, including the parabolic shape of  $\Psi = \Psi_{(\text{CMPA})}$  and the negative sensitivity of the functionalized Ti electrodes. First, the adsorption geometries of the MPA on the Au, Ti, and  $\text{TiO}_2$  slabs were calculated for both the standard thiol connection and the carboxyl connection. The Au(100) plane was chosen as a model plane because the XRD results of the studied materials suggest so (Figure S12). Adsorption simulations are also performed for the Au(111) plane for benchmarking purposes, though (Figure S13). Both Ti and  $\text{TiO}_2$  surfaces are considered because native passivation of the titanium plates may occur in an air atmosphere, potentially changing the chemistry and energetics of the MPA adsorption.

The adsorption geometries of the MPA via a standard thiol connection are given in Figure 3A–C with electron density

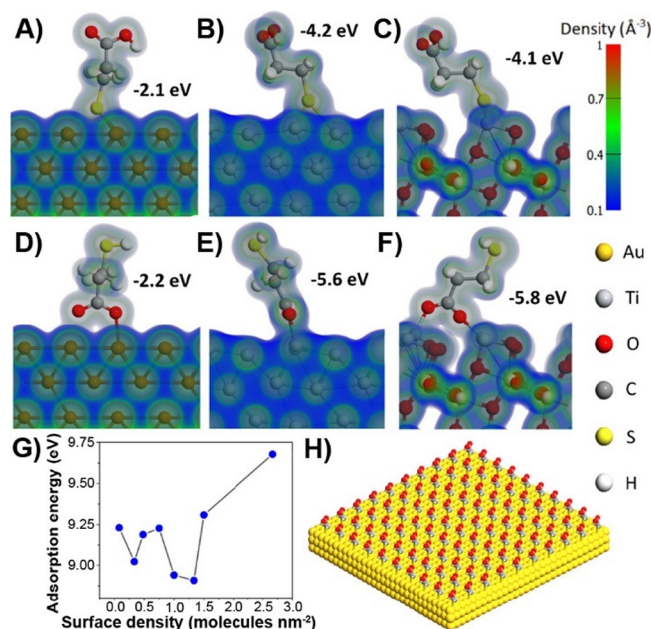


**Figure 3.** Adsorption geometry of the MPA molecule. Electron density maps illustrating the adsorption of MPA onto: (A) Au(100); (B) Ti(0001); and (C)  $\text{TiO}_2$  anatase (101) via standard thiol connection and: (D) Au(100); (E) Ti(0001); and (F)  $\text{TiO}_2$  anatase (101) via carboxyl group connection, respectively—numbers at each pane are adsorption energies; (G) adsorption energy changes with respect to the surface coverage of thiol-connected MPA on the gold surface; and (H) relaxed supercell geometry with optimal 1.33 molecules  $\text{nm}^{-2}$  grafting density of MPA.

maps drawn to highlight the intermolecular interactions. In all cases, well-known triangular bonding patterns with Au–S–Au and Ti–S–Ti are obtained.<sup>39</sup> The bond lengths are in the range of 2.4–2.6 Å with the S–Ti bond being the shortest (refer to SI, Table S2). All molecules are slightly tilted with respect to the surface, yet in all cases, the carboxyl group utilized for the further modification steps is pointed vertically. However, the adsorption energy calculated for the Au surface turns out to be the largest of all surfaces (–2.1 eV), and in the case of Ti and  $\text{TiO}_2$ , it is twice as large (–4.2 and –4.7 eV, respectively). Although this value is reasonable in comparison

to other reported thiol molecules,<sup>40</sup> the unexpected outcome indicates that the adsorption of thiol on the titanium surface or its oxide is more thermodynamically favorable than on the standard gold surface. On the other hand, the experiments presented in SI, Figure S4 showed that, contrary to gold or nanotextured electrodes, the modification of titanium does not lead to effective SARS-CoV-2 RBD recognition. Therefore, there must be a factor other than the adsorption of the MPA determining the functionalization success.

To solve this puzzle, an additional set of adsorption calculations was performed with an MPA molecule bonded to the surface, unconventionally, through the carboxyl group (Figure 3D–F). The result of the optimization on the Au surface is a five-membered ring of ...C–O–Au–Au–O... with two C–O–Au bonds of ca. 2.2 Å indicated by the electron density overlaps. The patterns obtained for the Ti and  $\text{TiO}_2$  surfaces are very similar with slightly shorter C–O–Ti bonds and distorted geometry on the anatase surface due to interactions with both titanium and oxygen atoms.

The most crucial observation is that, in all three cases, the adsorption energies are more negative for carboxyl linkage than for standard thiol linkage. In other words, the preferable and stronger binding pattern of the MPA molecule is through the carboxyl bond. However, while the difference between the adsorption energies of the two patterns is relatively small for gold (ca. 0.1 eV), it is high for Ti and its oxide (1.4 and 1.1 eV, respectively). This outcome is taken as the core of the explanation of the experimentally observed phenomena in the reasoning presented later on. Moreover, the universal force field molecular dynamics (UFF-MD) calculations were performed to verify the overtime stability of the modification for both types of linkage in the range of nanoseconds. They are contained in the SI file in Figures S9 and S10, and in general, strongly suggest that in both types of connections, MPA molecules retain similar conformations after 1 ns as predicted by static DFT.

Next, the whole modification was modeled and investigated using MM/MD approaches to understand why the sensitivity of the Ti sheet functionalization, measured by the impedance parameters, is negative, and to explicitly show the usefulness of the hemispherical AuNPs at the AuTi-NTE surface used in the experiment. First, the adsorption energies of the MPA molecules with different grafting densities were calculated (Figure 3G). The resulting curve has a minimum of 1.33 molecules  $\text{nm}^{-2}$ , indicating an optimal surface coverage of MPA molecules. This is similar to the experimentally obtained values for similar thiol molecules<sup>41</sup> but slightly lower because an ideally flat surface without adatoms was used in the model.<sup>42</sup> A graphical representation of the relaxed MPA surface density on a  $10 \times 10 \times 1$  supercell is given in Figure 3H. Additionally, a similar dependence of the adsorption energy dependence on the grafting density has been observed for the Au(111) crystallographic plane in an analogous simulation (see Figure S11).

Next, a CD147 was attached to this surface via an amide bond between the carboxyl group of the MPA and receptor's histidine moiety, and subsequently optimized with ReaxFF. Two projections of the resulting structure are given in Figure 4A showing a ca. 60° tilting angle between the protein and the gold surface. Moreover, the top view shows that one CD147 protein covers the area of ca. 60/100 MPA molecules. Therefore, even if there is a majority of the carboxyl-connected MPA molecules, it is still sufficient to create a compact surface



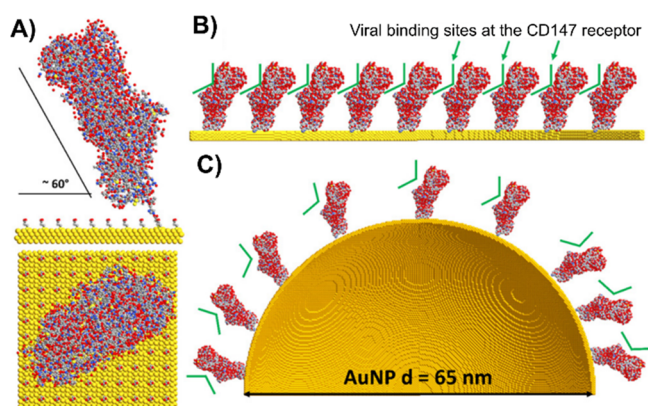


**Figure 4.** Adsorption of the CD147 receptor on the gold surface with MPA-EDC\_NHS functionalization. (A) Geometry of the CD147 receptor on the Au surface in two perpendicular projections—the tilt of the protein is marked black and equal to ca. 60°; (B and C) schematic illustration of 9 CD147 receptors on the flat gold and AuNP surfaces. Green segments indicate the place at the receptor for binding of the viral protein.

coverage with CD147 relevant for impedimetric sensing. Another observation is that the part of the molecule responsible for binding the viral protein (green marker in Figure 4) is exposed at the top of the receptor and similarly tilted. In other words, due to the attachment to the electrode surface, the viral binding site of the CD147 is not directly exposed, and the RBD has to undergo a particular 60° tilted orientation to be “caught” by the CD147 and for the sensing to occur efficiently.

However, the curved surface of the Au nanoparticle is a solution to this issue. This can be seen in an explicit graphical comparison of the functionalization with several CD147

molecules on flat and AuNP surfaces (Figure 4B,C). In the case of the flat surface, there is a binary choice between either a steric hindrance of the viral binding site or less grafting density, resulting in inefficient sensing. On the other hand, assuming the same number of CD147 molecules is adsorbed on both surfaces, no steric hindrance is observed on the AuNP and there is more space for the SARS-CoV-2 RBD to approach the receptors. Moreover, it is explicitly seen that the AuNP curvature allows higher conformational freedom for the CD147, which presumably is another reason for the facilitation of the sensing on the AuNP with respect to the flat surface.

Typically, the detection mechanism of the impedimetric sensors involves the increase of the charge transfer resistance  $R_{CT}$  by redox probes due to receptor-analyte-specific interactions. In the case of one-step quasi-reversible reactions, the general expression for the charge transfer resistance can be written as:<sup>43</sup>

$$R_{CT} = \frac{RT}{e^2 F^2 \alpha k_1 C_{ox}(0) + (1 - \alpha) k_2 C_{red}(0)} \quad (1)$$

where  $R$  and  $F$  are the gas constant and Faraday constant, respectively,  $e$  is the number of electrons transferred,  $T$  is the temperature,  $k_1$  and  $k_2$  are the forward and backward kinetic constants, respectively,  $\alpha$  is a charge transfer coefficient, and  $C_{ox}$  and  $C_{red}$  are the reagent concentrations at the surface (specifically, at the outer Helmholtz plane of the double layer<sup>44</sup>). In the case of complex reaction mechanisms, the expression is more complicated, but its general structure remains the same with the reciprocal relation between  $R_{CT}$  and kinetic constants. It should be noted that, during the experiment with changing the concentration of the analyte, the only variable quantities in the expression are  $C_{ox}$  and  $C_{red}$ . This is because the electrochemical reaction studied in the

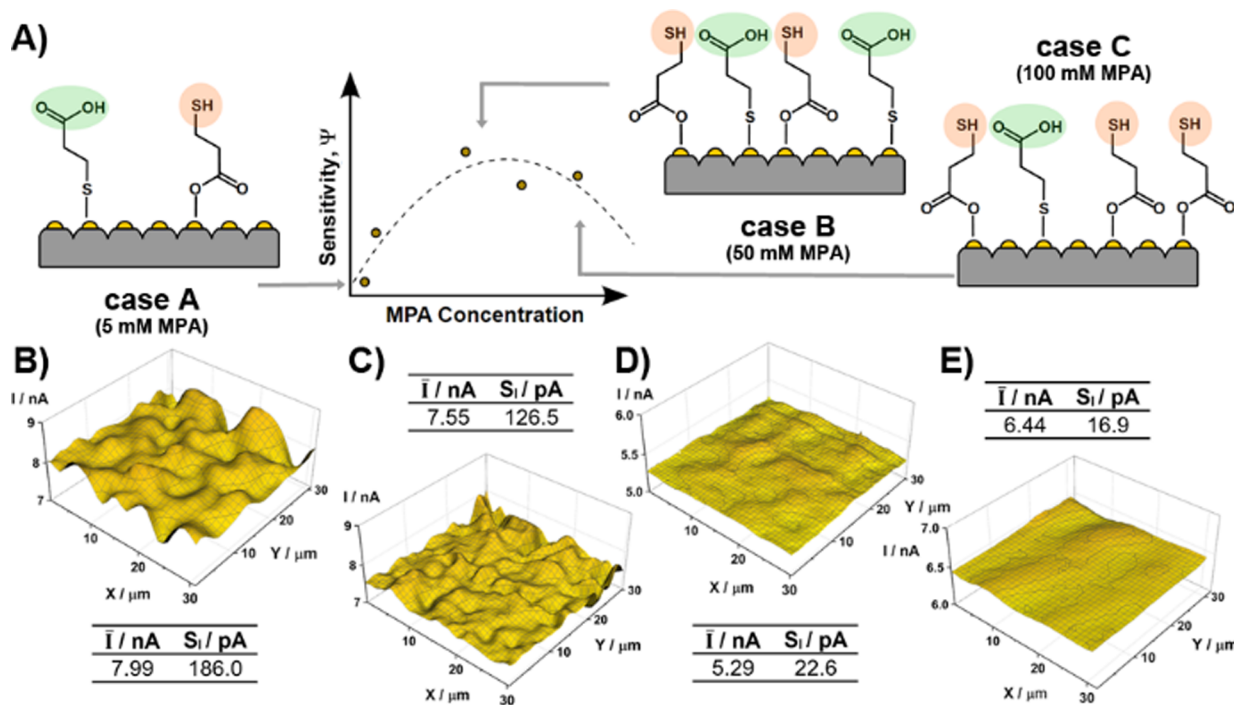


**Figure 5.** (A) Scheme explaining the correlation between the MPA concentration and sensor sensitivity  $\Psi$ ; (B–E) SECM maps of AuTi-NTE surface modified with different MPA concentrations: (B) 0 mM (bare), (C) 10 mM, (D) 50 mM, and (E) 100 mM. Microelectrode distance from the surface: 5  $\mu\text{m}$ .

experiment is the reduction and oxidation of ferrocyanides. The mechanism of those two reactions—and therefore  $\alpha$ ,  $k_1$ , and  $k_2$ —is presumably the same regardless of SARS-CoV2 RBD concentration. Therefore, the increase of  $R_{CT}$  must be equivalent to the plummet of the ferrocyanides surface concentration, which can be associated with the blocking of the available space “below” the CD147 (see Figure 4A) due to its conformation changes in contact with the RBD.

Those phenomena are anticipated to be responsible for the experimentally observed positive impedimetric sensitivity of the functionalization on solid Au and AuTi-NTE. However, in the case of the Ti sheet functionalization, negative sensitivity was observed (negative  $\Psi$  value in Figure 2E). This seemingly erroneous event is understandable because the majority, if not all, of the MPA molecules are attached to the Ti surface via carboxyl linkage. As a result of this flawed modification, the CD147 is bound only by dispersion vdW forces, not by a covalent bond. Assuming the RBD is capable of binding to the CD147, the conjunction presumably results in a partial detachment of the CD147 rather than blocking the surface available for the redox probe. Consequently,  $R_{CT}$  is smaller than the reference value measured after the addition of the BSA.

**3.4. Experimental Consequences of MPA Adsorption at the AuTi-NTE Surface.** In the case of MPA adsorption on the Ti surface, it is possible to explicitly write two rate eqs 2 and 3 describing the reactions of the thiol and carboxyl groups with the surface Ti atoms:

$$v_{\text{thiol}} = k^0_{\text{thiol}} \exp\left(\frac{4.2}{RT}\right) c(\theta)^m \quad (2)$$

$$v_{\text{carboxyl}} = k^0_{\text{carboxyl}} \exp\left(\frac{5.6}{RT}\right) c(\theta)^m \quad (3)$$

where  $c(\theta)^m$  is the concentration—surface coverage dependence given by the adsorption isotherm (elaboration on the mathematics of those isotherms can be found in SI, Section 7), and  $k^0$  is the rate constants of the MPA reaction with gold. The numbers in the exponents equal to 4.2 and 5.6 eV correspond to the adsorption energies calculated by DFT. Assuming the adsorption isotherms are the same because it is the same molecule adsorbing, one can immediately state that the adsorption of the MPA molecule via a carboxyl connection is faster than adsorption via a thiol connection with an exponential factor determined by the difference between adsorption energies (1.4 eV). However, in the case of MPA adsorption on the Au surface, the energy difference between the thiol and carboxyl connections is relatively small (ca. 0.1 eV), indicating that carboxyl connections are only mildly more probable than thiol connections. Thus, when the concentration of the MPA in the solution is low and the surface coverage determined by the isotherm is not saturated, presumably both bonding patterns are possible (Figure 5A, case A) on the Au surface. When the bulk concentration of MPA is larger, the surface coverage of thiol-connected MPA is also higher and the degree of successful CD147 modification is also higher, resulting in enhanced RBD detection sensitivity on Au surfaces. This trend continues with the increasing MPA concentration until the vertex of the parabola is reached, presumably approximately when  $c_{\text{MPA}}$  is sufficient for full electrode surface coverage ( $\theta = 100\%$ ) with the adsorbed monolayer (Figure 5A, case B), which corresponds to the optimal coverage of the thiol-connected MPA. Here, the

resulting geometry of the attached CD147 is optimal for sensing purposes. For the MPA concentrations exceeding the optimum, displacement of the thiol-connected MPA to carboxyl-connected MPA is anticipated to take place (Figure 5A, case C). Despite the highest MPA surface coverage, the degree of successful CD147 modifications is smaller because according to the rate equations, more MPA is bonded through carboxyl linkage, which does not result in a proper CD147 attachment. Therefore, for the highest MPA concentrations, the sensitivity decreases on both Au and Au–Ti surfaces.

On the other hand, the SARS-CoV-2 RBD detection using Ti electrodes is ineffective because all MPA molecules are carboxyl-connected even at the lowest MPA concentrations due to the significantly higher difference between the adsorption energy of the two bonding patterns influencing the rate equations. This is also experimentally confirmed by XPS spectra in Figures 1H and S1D by the presence of Ti–C and free SH moieties, as well as an absence of S–Me bonding.

SECM imaging was performed for further experimental proof of the hypothesized influence of MPA on the electrochemical response. The maps recorded at bare AuTi-NTEs and after modification using different  $c_{\text{MPA}}$  are presented in Figure 5B,C–E, respectively. The approach curves registered at the beginning of each SECM measurement can be found in SI, Figure S6. Analyzing the shape of the SECM maps allowed us to calculate the average current registered at the tip of the microelectrode  $\bar{I}$  and the current distortion  $S_I$  describing the profile height deviations, and defined by eq 4:<sup>45</sup>

$$S_I = \sqrt{\frac{1}{N} \sum_{x,y} h_{(x,y)}^2} \quad (4)$$

and corresponding to the standard deviation of the height on the SECM maps with the number of pixels equal to  $N$ . Both  $\bar{I}$  and  $S_I$  parameters are presented in the inset tables within Figure 5.

The SECM data analysis shows that the highest current (7.99 nA) was registered at the tip of the microelectrode  $\bar{I}$  located above the unmodified AuTi-NTE surface. Increasing  $c_{\text{MPA}}$  up to 50 mM leads to a consecutive linear decrease in the registered currents. The analogous decrease is also observed in control experiments, where standard CV curves of Au, Au–Ti-NTE, and Ti surfaces were registered in the presence of ferrocyanides (SI, Figure S7).

The explanation for the current decrease with  $c_{\text{MPA}}$  is twofold. First, the adsorption of MPA molecules at the electrode surface forms a diffusion barrier, lowering the  $\text{Fe}(\text{CN})_6^{3-}$  transport rate and the measured current. Second, there is an additional kinetic inhibition lowering  $k^0$  due to the presence of the flawed MPA attachment via carboxyl linkage. Previously discussed arguments from the DFT have shown that the inverse configuration is especially abundant in the case of Ti and  $\text{TiO}_2$  surfaces with high MPA concentrations (eqs 2 and 3). To corroborate the kinetic inhibition, a set of DFT calculations involving interactions of the ferrocyanide molecule with MPA-modified surfaces was performed. In the SI, Movies S1 and S2 show geometry optimization trajectories where a ferrocyanide anion is initially placed above the Au surface covered with a thermodynamic grafting density of the MPA with proper thiol linkage and flawed carboxyl linkage. It is easy to see that the carboxyl groups of the thiol-linked MPA molecules pull the ferrocyanide redox marker toward the surface, facilitating adsorption, where the final Fe–Au distance

(at the configuration in the free energy minimum) is equal to 3.0 Å. On the other hand, this effect is not manifested in the case of carboxyl-linked MPA molecules, and the final Fe–Au distance is equal to 4.2 Å—see the comparison of the last frames of the optimizations in Figure S8. As a result, the flawed modification abundant on the Ti electrode and slightly prevalent in the AuTi-NTE leads to the decrease in the faradaic ferrocyanide currents in Figure S7 and microelectrode tip current in the SECM measurements.

However, exceeding  $c_{\text{MPA}} = 50$  mM, there is a slight increase in the microelectrode current. The profound nature of this phenomenon is unclear; however, it can presumably be correlated with the creation of a nonspecifically adsorbed multilayered and nonhomogeneous film of MPA molecules, which results in a significantly different diffusion field. Presumably, when  $c_{\text{MPA}}$  exceeds a certain threshold above 50 mM, the geometry of the diffusion field begins to resemble the microelectrode array case rather than a flat surface, which is known to increase the steady-state currents.<sup>46,47</sup> A similar phenomenon was recently reported by our group during the modification of boron-doped carbon nanowalls with zwitterionic polymers.<sup>48</sup> In this study, the above-mentioned shift in the diffusional field after modification was pronounced to a large extent, so the currents increased several times regardless of the value of kinetic constant  $k^0$ . In the following study, the current change induced by the overload of MPA is less intensive, but presumably reflects the same phenomenon—on the one hand, inverse modification reduces the current, and on the other, the diffusion field geometry increases them after a certain degree of inhomogeneity (measured by  $S_I$ ) is achieved.

Free Ti sites might be present at the AuTi-NTE surface due to the fact that adsorption–desorption is an equilibrium process, and some regions of the electrode surface remain unmodified in the absence of the reagent. The complete surface coverage is not necessary to achieve the described parabolic effect of MPA concentration influence on sensor sensitivity, as the CD147 protein is a large molecule that can cover approximately 60 out of 100 MPA molecules when appropriately linked to a single MPA molecule. Nevertheless, the absence of an electrochemical response (denoting negative sensor performance) in the Ti sheet electrode following its exposure to SARS-CoV-2 RBD signifies that the carboxyl-bonded MPA is adsorbed at the Ti surface, preventing direct anchoring of the CD147 receptor.

#### 4. CONCLUSIONS

Herein, we proposed a novel sensing platform based on a nanostructured titania substrate with embedded gold nanoparticles (AuTi-NTE). The successful functionalization covering several steps, including MPA adsorption, and EDC/NHC coupling was recognized via XPS. According to the spectra, the MPA adsorbs onto the Au and Ti ( $\text{TiO}_2$ ). The modification procedure was also monitored via successive electrochemical measurements.

One must pay special attention to the functionalization agent and the type of bonding formed. Our results indicate that the MPA concentration is the key parameter in terms of biosensor efficacy. The studies performed made it possible to select the most optimal concentration of mercaptopropionic acid, which was 50 mM in the case of AuTi-NTE. A DFT simulation was carried out to analyze the nature of the modification mechanism in detail. It was shown that functionalization by MPA is preferable by the carboxyl group

over the thiol, whatever the type of substrate. The formation of covalent Au–S bonding is required to successfully carry out the consecutive functionalization steps. The modeling using MM/MD approaches indicates that even if there is a majority of the carboxyl-connected MPA molecules, it is still sufficient to form CD147 compact coverage relevant for impedimetric sensing. However, exceeding the optimal MPA concentration is a dominant contributor to improper carboxyl bonding and decreases the overall biosensor efficacy. The DFT findings were supported here by the experimental data collected using a scanning electrochemical microscope, as well as XPS.

A five times higher response toward the SARS-CoV-2 RBD protein was obtained for AuTi-NTE when compared to a flat Au electrode, where the curved shape of gold nanostructures is crucial for CD147 conformational freedom. The AuTi-NTE preparation can be easily scaled-up and commercialized since used compounds are readily available, the process is reproducible, and only a tiny amount of gold is required, thus offering a great alternative for the formation of gold nanoparticles with other methods.

#### ■ ASSOCIATED CONTENT

##### SI Supporting Information

The Supporting Information is available free of charge at <https://pubs.acs.org/doi/10.1021/acs.jpcc.3c00697>.

The file contains XPS spectra (Au 4f, Ti 2p, N 1s, C 1s) for modified electrodes with discussion, EIS and CV results for functionalized electrodes,  $R_{\text{CT}}$  changes of AuTi-NTE with MPA concentration, SEM binarized image, computational details, and additional DFT results, SECM approach curves, adsorption isotherms discussion (PDF)

#### ■ AUTHOR INFORMATION

##### Corresponding Author

Jacek Ryl – *Institute of Nanotechnology and Materials Engineering and Advanced Materials Center, Gdańsk University of Technology, Gdańsk 80-233, Poland;*  
✉ [orcid.org/0000-0002-0247-3851](mailto:jacek.ryl@pg.edu.pl); Email: [jacek.ryl@pg.edu.pl](mailto:jacek.ryl@pg.edu.pl)

##### Authors

Wiktoria Lipińska – *Centre for Plasma and Laser Engineering, The Szewalski Institute of Fluid-Flow Machinery, Polish Academy of Sciences, Gdańsk 80-231, Poland*

Adrian Olejnik – *Centre for Plasma and Laser Engineering, The Szewalski Institute of Fluid-Flow Machinery, Polish Academy of Sciences, Gdańsk 80-231, Poland; Department of Metrology and Optoelectronics, Faculty of Electronics, Telecommunications and Informatics, Gdańsk University of Technology, Gdańsk 80-233, Poland*

Monika Janik – *Department of Metrology and Optoelectronics, Faculty of Electronics, Telecommunications and Informatics, Gdańsk University of Technology, Gdańsk 80-233, Poland; Institute of Microelectronics and Optoelectronics, Faculty of Electronics and Information Technology, Warsaw University of Technology, Warsaw 00-662, Poland*

Mateusz Brodowski – *Institute of Nanotechnology and Materials Engineering and Advanced Materials Center, Gdańsk University of Technology, Gdańsk 80-233, Poland*



Karolina Sapięga – Institute of Nanotechnology and Materials Engineering and Advanced Materials Center, Gdańsk University of Technology, Gdańsk 80-233, Poland

Mattia Pierpaoli – Department of Metrology and Optoelectronics, Faculty of Electronics, Telecommunications and Informatics, Gdańsk University of Technology, Gdańsk 80-233, Poland; [orcid.org/0000-0002-7508-1824](https://orcid.org/0000-0002-7508-1824)

Katarzyna Siuzdak – Centre for Plasma and Laser Engineering, The Szewalski Institute of Fluid-Flow Machinery, Polish Academy of Sciences, Gdańsk 80-231, Poland; [orcid.org/0000-0001-7434-6408](https://orcid.org/0000-0001-7434-6408)

Robert Bogdanowicz – Department of Metrology and Optoelectronics, Faculty of Electronics, Telecommunications and Informatics, Gdańsk University of Technology, Gdańsk 80-233, Poland

Complete contact information is available at:

<https://pubs.acs.org/10.1021/acs.jpcc.3c00697>

### Author Contributions

Conceptualization: K.S., R.B., and J.R., methodology: A.O. and J.R., validation: A.O. and M.B., formal analysis: W.L. and A.O., investigation: W.L., M.B., K.S., and J.R., resources: W.L., M.J., and K.S., data curation: W.L. and A.O., writing-original draft: W.L., A.O., M.B., K.S., K.S., R.B., and J.R., writing-review and editing: M.J., M.P., K.S., R.B., and J.R., visualization: A.O., M.P., and J.R., supervision: J.R., funding acquisition J.R.

### Notes

The authors declare no competing financial interest.

### ACKNOWLEDGMENTS

This work was partially supported by the National Science Centre (Republic of Poland) under Project 2020/37/B/ST7/03262. The support of the Rector of the Gdańsk University of Technology to equip the scanning electrochemical microscopy laboratory is greatly acknowledged. K.S. appreciates support from the National Science Centre (Republic of Poland) under the CEUS-UNISONO Project 2020/02/Y/ST8/00030.

### REFERENCES

- Cesewski, E.; Johnson, B. N. Electrochemical Biosensors for Pathogen Detection. *Biosens. Bioelectron.* **2020**, *159*, No. 112214.
- Felix, F. S.; Angnes, L. Electrochemical Immunosensors – A Powerful Tool for Analytical Applications. *Biosens. Bioelectron.* **2018**, *102*, 470–478.
- Lim, S. A.; Ahmed, M. U. Introduction to Immunosensors. In *Detection Science*; Ahmed, M. U.; Zourob, M.; Tamiya, E., Eds.; Royal Society of Chemistry: Cambridge, 2019; pp 1–20.
- Danvirutai, P.; Ekpanyapong, M.; Tuantranont, A.; Bohez, E.; Anutrakulchai, S.; Wisitsoraat, A.; Srichan, C. Ultra-Sensitive and Label-Free Neutrophil Gelatinase-Associated Lipocalin Electrochemical Sensor Using Gold Nanoparticles Decorated 3D Graphene Foam towards Acute Kidney Injury Detection. *Sens. Bio-Sens. Res.* **2020**, *30*, No. 100380.
- Blair, E. O.; Corrigan, D. K. A Review of Microfabricated Electrochemical Biosensors for DNA Detection. *Biosens. Bioelectron.* **2019**, *134*, 57–67.
- Wang, J. Electrochemical Glucose Biosensors. *Chem. Rev.* **2008**, *108*, 814–825.
- Matharu, Z.; Bandodkar, A. J.; Gupta, V.; Malhotra, B. D. Fundamentals and Application of Ordered Molecular Assemblies to Affinity Biosensing. *Chem. Soc. Rev.* **2012**, *41*, 1363–1402.
- Tajima, N.; Takai, M.; Ishihara, K. Significance of Antibody Orientation Unraveled: Well-Oriented Antibodies Recorded High Binding Affinity. *Anal. Chem.* **2011**, *83*, 1969–1976.

(9) Welch, N. G.; Scoble, J. A.; Muir, B. W.; Pigram, P. J. Orientation and Characterization of Immobilized Antibodies for Improved Immunoassays (Review). *Biointerphases* **2017**, *12*, No. 02D301.

(10) Kim, H. J.; Park, D.; Park, Y.; Kim, D.-H.; Kim, J. Electric-Field-Mediated In-Sensor Alignment of Antibody's Orientation to Enhance the Antibody–Antigen Binding for Ultrahigh Sensitivity Sensors. *Nano Lett.* **2022**, *22*, 6537–6544.

(11) Jolly, P.; Zhuravski, P.; Hammond, J. L.; Miodęk, A.; Liébana, S.; Bertok, T.; Tkáč, J.; Estrela, P. Self-Assembled Gold Nanoparticles for Impedimetric and Amperometric Detection of a Prostate Cancer Biomarker. *Sens. Actuators, B* **2017**, *251*, 637–643.

(12) Singh, S.; Gill, A. A. S.; Nlooto, M.; Karpooomath, R. Prostate Cancer Biomarkers Detection Using Nanoparticles Based Electrochemical Biosensors. *Biosens. Bioelectron.* **2019**, *137*, 213–221.

(13) Sun, X.; Luo, Y.; Liao, F.; Lu, W.; Chang, G. Novel Nanotextured Microelectrodes: Electrodeposition-Based Fabrication and Their Application to Ultrasensitive Nucleic Acid Detection. *Electrochim. Acta* **2011**, *56*, 2832–2836.

(14) Bhattacharya, A.; Rao, V. P.; Jain, C.; Ghose, A.; Banerjee, S. Bio-Sensing Property of Gold Coated ZnO Nanorods. *Mater. Lett.* **2014**, *117*, 128–130.

(15) Song, Z.; Yuan, R.; Chai, Y.; Yin, B.; Fu, P.; Wang, J. Multilayer Structured Amperometric Immunosensor Based on Gold Nanoparticles and Prussian Blue Nanoparticles/Nanocomposite Functionalized Interface. *Electrochim. Acta* **2010**, *55*, 1778–1784.

(16) Wei, N.; Xin, X.; Du, J.; Li, J. A Novel Hydrogen Peroxide Biosensor Based on the Immobilization of Hemoglobin on Three-Dimensionally Ordered Macroporous (3DOM) Gold-Nanoparticle-Doped Titanium Dioxide (GTD) Film. *Biosens. Bioelectron.* **2011**, *26*, 3602–3607.

(17) Lipińska, W.; Ryl, J.; Slepski, P.; Siuzdak, K.; Grochowska, K. Exploring Multi-Step Glucose Oxidation Kinetics at GOx-Functionalized Nanotextured Gold Surfaces with Differential Impedimetric Technique. *Measurement* **2021**, *174*, No. 109015.

(18) Lipińska, W.; Siuzdak, K.; Karczewski, J.; Dołęga, A.; Grochowska, K. Electrochemical Glucose Sensor Based on the Glucose Oxidase Entrapped in Chitosan Immobilized onto Laser-Processed Au-Ti Electrode. *Sens. Actuators, B* **2021**, *330*, No. 129409.

(19) Russo, M. J.; Han, M.; Desroches, P. E.; Manasa, C. S.; Dennaoui, J.; Quigley, A. F.; Kapsa, R. M. I.; Moulton, S. E.; Guijt, R. M.; et al. Antifouling Strategies for Electrochemical Biosensing: Mechanisms and Performance toward Point of Care Based Diagnostic Applications. *ACS Sens.* **2021**, *6*, 1482–1507.

(20) Laforgue, A.; Addou, T.; Bélanger, D. Characterization of the Deposition of Organic Molecules at the Surface of Gold by the Electrochemical Reduction of Aryldiazonium Cations. *Langmuir* **2005**, *21*, 6855–6865.

(21) Aschwanden, L.; Mallat, T.; Maciejewski, M.; Krumeich, F.; Baiker, A. Development of a New Generation of Gold Catalysts for Amine Oxidation. *ChemCatChem* **2010**, *2*, 666–673.

(22) Chen, S.; Kimura, K. Synthesis and Characterization of Carboxylate-Modified Gold Nanoparticle Powders Dispersible in Water. *Langmuir* **1999**, *15*, 1075–1082.

(23) Vericat, C.; Vela, M. E.; Benitez, G.; Carro, P.; Salvarezza, R. C. Self-Assembled Monolayers of Thiols and Dithiols on Gold: New Challenges for a Well-Known System. *Chem. Soc. Rev.* **2010**, *39*, 1805.

(24) Singh, S.; Kaushal, A.; Khare, S.; Kumar, P.; Kumar, A. Gold–Mercaptopropionic Acid–Polyethylenimine Composite Based DNA Sensor for Early Detection of Rheumatic Heart Disease. *Analyst* **2014**, *139*, 3600–3606.

(25) Loaiza, Ó. A.; Campuzano, S.; Prada, A. G.-V.; Pedrero, M.; Pingarrón, J. M. Amperometric DNA Quantification Based on the Use of Peroxidase-Mercaptopropionic Acid-Modified Gold Electrodes. *Sens. Actuators, B* **2008**, *132*, 250–257.

(26) Gao, F.; Han, L. Implementing the Nelder-Mead Simplex Algorithm with Adaptive Parameters. *Comput. Optim. Appl.* **2012**, *51*, 259–277.

- (27) Niedziakowski, P.; Slepski, P.; Wysocka, J.; Chamier-Cieminska, J.; Burczyk, L.; Sobaszek, M.; Wcislo, A.; Ossowski, T.; Bogdanowicz, R.; Ryl, J. Multisine Impedimetric Probing of Biocatalytic Reactions for Label-Free Detection of DEFB1 Gene: How to Verify That Your Dog Is Not Human? *Sens. Actuators, B* **2020**, *323*, No. 128664.
- (28) Brodowski, M.; Pierpaoli, M.; Janik, M.; Kowalski, M.; Ficek, M.; Slepski, P.; Trzaskowski, B.; Swain, G.; Ryl, J.; Bogdanowicz, R. Enhanced Susceptibility of SARS-CoV-2 Spike RBD Protein Assay Targeted by Cellular Receptors ACE2 and CD147: Multivariate Data Analysis of Multisine Impedimetric Response. *Sens. Actuators, B* **2022**, *370*, No. 132427.
- (29) Battocchio, C.; Porcaro, F.; Mukherjee, S.; Magnano, E.; Nappini, S.; Fratoddi, I.; Quintiliani, M.; Russo, M. V.; Polzonetti, G. Gold Nanoparticles Stabilized with Aromatic Thiols: Interaction at the Molecule–Metal Interface and Ligand Arrangement in the Molecular Shell Investigated by SR-XPS and NEXAFS. *J. Phys. Chem. C* **2014**, *118*, 8159–8168.
- (30) Niedziakowski, P.; Bojko, M.; Ryl, J.; Wcislo, A.; Spodzieja, M.; Magiera-Mularz, K.; Guzik, K.; Dubin, G.; Holak, T. A.; Ossowski, T.; Rodziewicz-Motowidlo, S. Ultrasensitive Electrochemical Determination of the Cancer Biomarker Protein SPD-L1 Based on a BMS-8-Modified Gold Electrode. *Bioelectrochemistry* **2021**, *139*, No. 107742.
- (31) Nilsson, D.; Watcharinanon, S.; Eng, M.; Li, L.; Moons, E.; Johansson, L. S. O.; Zharnikov, M.; Shaporenko, A.; Albinsson, B.; Mårtensson, J. Characterization of Self-Assembled Monolayers of Oligo(Phenyleneethynylene) Derivatives of Varying Shapes on Gold: Effect of Laterally Extended  $\pi$ -Systems. *Langmuir* **2007**, *23*, 6170–6181.
- (32) Alkathiri, T.; Xu, K.; Zhang, B. Y.; Khan, M. W.; Jannat, A.; Syed, N.; Almutairi, A. F. M.; Ha, N.; Alsaif, M. M. Y. A.; Pillai, N.; et al. 2D Palladium Sulphate for Visible-Light-Driven Optoelectronic Reversible Gas Sensing at Room Temperature. *Small Sci.* **2022**, *2*, No. 2100097.
- (33) Bagiyani, G. A.; Koroleva, I. K.; Soroka, N. V.; Ufimtsev, A. V. Oxidation of Thiol Compounds by Molecular Oxygen in Aqueous Solutions. *Russ. Chem. Bull.* **2003**, *52*, 1135–1141.
- (34) Cant, D. J. H.; Syres, K. L.; Lunt, P. J. B.; Radtke, H.; Treacy, J.; Thomas, P. J.; Lewis, E. A.; Haigh, S. J.; O'Brien, P.; Schulte, K.; et al. Surface Properties of Nanocrystalline PbS Films Deposited at the Water–Oil Interface: A Study of Atmospheric Aging. *Langmuir* **2015**, *31*, 1445–1453.
- (35) Le, C. M. Q.; Morlet-Savary, F.; Chemtob, A. Role of Thiol Oxidation by Air in the Mechanism of the Self-Initiated Thermal Thiol–Ene Polymerization. *Polym. Chem.* **2021**, *12*, 6594–6605.
- (36) Bahadır, E. B.; Sezgintürk, M. K. A Review on Impedimetric Biosensors. *Artif. Cells Nanomed. Biotechnol.* **2016**, *44*, 248–262.
- (37) Lipińska, W.; Grochowska, K.; Siuzdak, K. Enzyme Immobilization on Gold Nanoparticles for Electrochemical Glucose Biosensors. *Nanomaterials* **2021**, *11*, 1156.
- (38) Konieczka, P.; Namieśnik, J. *Quality Assurance and Quality Control in the Analytical Chemical Laboratory: A Practical Approach*, 2nd edition; CRC Press, 2018.
- (39) Häkkinen, H. The Gold–Sulfur Interface at the Nanoscale. *Nat. Chem.* **2012**, *4*, 443–455.
- (40) Peiretti, L. F.; Quaino, P.; Tielens, F. Competition between Two High-Density Assemblies of Poly(Phenyl)Thiols on Au(111). *J. Phys. Chem. C* **2016**, *120*, 25462–25472.
- (41) Hinterwirth, H.; Kappel, S.; Waitz, T.; Prohaska, T.; Lindner, W.; Lämmerhofer, M. Quantifying Thiol Ligand Density of Self-Assembled Monolayers on Gold Nanoparticles by Inductively Coupled Plasma–Mass Spectrometry. *ACS Nano* **2013**, *7*, 1129–1136.
- (42) Azzam, W.; Al-Rashdi, A.; Subaihi, A.; Rohwerder, M.; Zharnikov, M.; Bashir, A. Annealing Effect for Self-Assembled Monolayers Formed from Terphenylethanethiol on Au(111). *Phys. Chem. Chem. Phys.* **2020**, *22*, 13580–13591.
- (43) Lasia, A. *Electrochemical Impedance Spectroscopy and Its Applications*; Springer: New York, 2014.
- (44) Bard, A. J.; Faulkner, L. R. *Electrochemical Methods: Fundamentals and Applications*, 2nd edition; Wiley: New York, 2001.
- (45) Niedziakowski, P.; Koterwa, A.; Olejnik, A.; Zielinski, A.; Gornicka, K.; Brodowski, M.; Bogdanowicz, R.; Ryl, J. Deciphering the Molecular Mechanism of Substrate-Induced Assembly of Gold Nanocube Arrays toward an Accelerated Electrocatalytic Effect Employing Heterogeneous Diffusion Field Confinement. *Langmuir* **2022**, *38*, 9597–9610.
- (46) Compton, R. G.; Kätelhön, E.; Ward, K. R.; Laborda, E. *Understanding Voltammetry: Simulation of Electrode Processes*, 2nd edition; World Scientific: New Jersey, 2020.
- (47) *Nanomaterials for Electrochemical Sensing and Biosensing*; Pumera, M., Ed.; Pan Stanford Publishing: Singapore, 2014.
- (48) Olejnik, A.; Ficek, M.; Szkodo, M.; Stanisławska, A.; Karczewski, J.; Ryl, J.; Dołęga, A.; Siuzdak, K.; Bogdanowicz, R. Tailoring Diffusional Fields in Zwitterion/Dopamine Copolymer Electropolymerized at Carbon Nanowalls for Sensitive Recognition of Neurotransmitters. *ACS Nano* **2022**, *16*, 13183–13198.